145 (2023) 213250

Contents lists available at ScienceDirect

Biomaterials Advances

journal homepage: www.journals.elsevier.com/materials-science-and-engineering-c

Rapid fabrication and screening of tailored functional 3D biomaterials: Validation in bone tissue repair – Part II

Antonio Conde-González [a,1], Michael Glinka [b,1], Deepanjalee Dutta [a,1], Robert Wallace [c], Anthony Callanan [d], Richard O.C. Oreffo [b,*], Mark Bradley [a,*]

[a] EaStCHEM School of Chemistry, University of Edinburgh, Edinburgh EH9 3FJ, UK
[b] Bone and Joint Research Group, Centre for Human Development, Stem Cells and Regeneration, Faculty of Medicine, University of Southampton, Southampton SO16 6YD, UK
[c] Orthopaedics and Trauma, University of Edinburgh, Edinburgh EH16 4SB, UK
[d] School of Engineering, Institute for Bioengineering, University of Edinburgh, Edinburgh EH9 3DW, UK

ARTICLE INFO

Keywords:
3D scaffolds
Biomaterials
High throughput
Tissue engineering
Bone
Angiogenesis

ABSTRACT

Regenerative medicine strategies place increasingly sophisticated demands on 3D biomaterials to promote tissue formation at sites where tissue would otherwise not form. Ideally, the discovery/fabrication of the 3D scaffolds needs to be high-throughput and uniform to ensure quick and in-depth analysis in order to pinpoint appropriate chemical and mechanical properties of a biomaterial. Herein we present a versatile technique to screen new potential biocompatible acrylate-based 3D scaffolds with the ultimate aim of application in tissue repair. As part of this process, we identified an acrylate-based 3D porous scaffold that promoted cell proliferation followed by accelerated tissue formation, pre-requisites for tissue repair. Scaffolds were fabricated by a facile freeze-casting and an *in-situ* photo-polymerization route, embracing a high-throughput synthesis, screening and characterization protocol. The current studies demonstrate the dependence of cellular growth and vascularization on the porosity and intrinsic chemical nature of the scaffolds, with tuneable 3D scaffolds generated with large, interconnected pores suitable for cellular growth applied to skeletal reparation. Our studies showed increased cell proliferation, collagen and ALP expression, while chorioallantoic membrane assays indicated biocompatibility and demonstrated the angiogenic nature of the scaffolds. VEGRF2 expression *in vivo* observed throughout the 3D scaffolds in the absence of growth factor supplementation demonstrates a potential for angiogenesis. This novel platform provides an innovative approach to 3D scanning of synthetic biomaterials for tissue regeneration.

1. Introduction

Tissue regenerative therapies necessitate the temporal and coordinated control of stem and progenitor cells. To achieve this, synthetic polymer scaffolds have been explored as substrates for supporting stem and progenitor cell growth and function [1]. For example, acrylate-based scaffolds have found wide applications in musculoskeletal regeneration including regeneration of cartilage, with evidence of excellent tissue regeneration three months post-implantation [2]. Moreover, acrylate coatings have been shown to enhance endothelial coverage and improve biomechanical properties of vascular grafts [3]. To develop polymer scaffolds that meet tissue specific prerequisites such as cell maintenance, provide appropriate biochemical cues and induce vasculature formation, high-throughput production and screening of novel biomaterials becomes a prerequisite. Recent efforts in this direction include the application of inkjet fabrication of arrays of thousands of acrylate-based polymers for the discovery of substrates that support the culture of human embryonic stem cells [4–7] and polymer blend evaluation for the discovery of materials that support the growth and differentiation of STRO-1+ human skeletal stem and osteoprogenitor populations [8].

A central challenge associated with an implanted scaffold resides in the scaffold association with the host tissue vasculature. Scaffold-tissue integration is mediated, in part, by the presence of endothelial cells on the lining of the blood vessels, which secrete growth factors that promote angiogenesis, a prerequisite for tissue regeneration to occur [9].

* Corresponding authors.
E-mail addresses: Richard.Oreffo@soton.ac.uk (R.O.C. Oreffo), Mark.Bradley@ed.ac.uk (M. Bradley).
[1] These authors contributed equally.

https://doi.org/10.1016/j.bioadv.2022.213250
Received 11 July 2022; Received in revised form 24 November 2022; Accepted 13 December 2022
Available online 16 December 2022

Indeed, in the formation of new bone and the reparation of local skeletal injuries (fracture), the vasculature plays a significant role in supporting cell recruitment, maintenance and directed cell differentiation facilitating repair. Furthermore, in bone regeneration, blood vessels supplying oxygen and nutrients, remove toxic components and, additionally, serve as a reservoir for pericytes and osteoblasts, which further support and induce cell differentiation [10]. The appropriate surface chemistry and mechanical properties offered by porous scaffolds thus becomes important in directing such tissue repair through angiogenesis and tissue regeneration [11,12]. Optimum bone regeneration in concert with vasculature formation requires that the scaffolds display a range of interconnected pores that correspond to the size of the trabeculae (100 to 400 μm), as these pore sizes facilitate and stimulate proliferation and osteogenesis (100 to 200 μm) along with angiogenesis (200 to 400 μm) [7,13–15]. In addition a plethora of studies have harnessed scaffolds loaded with growth factors such as BMP-2 and VEGF to facilitate tissue regeneration [16–18]. However, to date, few studies have explored the fabrication of a potent synthetic biomaterial with the potential to facilitate growth factor-free angiogenesis and tissue formation.

This study is based on previously developed high-throughput techniques allowing an efficient fabrication approach to generate libraries of 3D polymer scaffolds *via* freeze-casting and photo-polymerization for studying cell-material interactions and screening functional polymeric biomaterials [19]. This facile process accelerates the development of new biomaterials for potential tissue regeneration, harnessing *in situ* photo-polymerization to explore a variety of monomer combinations for the formation of porous 3D scaffolds. It is a unique approach compared to previous reports, where pre-synthesized polymers were used in the production of scaffolds [20–22]. Most of the high throughput techniques developed, even the most recently reported approaches presented by Revia and *co*-workers where an automated dispensing platform was used for high throughput 3D scaffold preparation, centre around the idea of casting pre-synthesized polymer solutions into multi-well plates. In the present study we present a novel method to synthesize the polymer scaffolds in a multi-well format. This reduces artifacts introduced during transfer of a preformed polymer scaffold onto a well plate using dispensing techniques [23]. Such a high throughput technique presented in this current study provides an advantage over other methods such as 3D printing as it facilitates a thorough investigation of cell behaviour in a three-dimensional environment with highly controlled porosity, often lacking in 3D printing techniques [7,24].

Herein, we improvise on the developed technique by testing the growth and cell behaviour of human fetal bone marrow stromal cells (FBMSCs) over the osteosarcoma cell line (SAOS-2) used in the original study [19] to provide clinically relevant conditions and determine the biocompatibility of the synthetic polymer scaffolds. Further, based on the *in vitro* cell culture studies selected polymer scaffolds were explored in an *ex vivo* CAM assay and *in vivo* studies to determine their potential using preclinical models. The new 3D scaffolds promoted cellular proliferation and showed preliminary vasculature formation penetration throughout the entire scaffold structure. The intrinsic properties of the scaffolds, together with the characteristics of the porous network, were central in facilitating and accounting for their proangiogenic nature. The subsequent stimulation of osteoblastic differentiation of the human fetal bone marrow stromal cells (FBMSCs) indicated scaffolds which would be applicable to bone repair. This is a key finding of the current work where the polymer scaffolds were able to maintain cells and promote preliminary vasculature formation in the absence of any applied exogenous growth factors.

The current study explores the application of the most promising polymer scaffolds which were selected based on the original combinatorial screening study performed by Conde-González [19]. The fabrication process explored a variety of novel polyacrylates and 3D microstructures that were interrogated using a robust 3D screening methodology employing FBMSCs. FBMSCs were selected for evaluation given their highly proliferative nature and demonstrated multipotentiality to differentiate along the various stromal lineages [25]. High porosity scaffolds that supported 3D cell proliferation and facilitated the expression of high levels of collagen, and displayed mechanical properties comparable to native musculoskeletal tissue, were identified. In addition, the identified scaffolds demonstrated, uniquely, substantial integration within the chick chorioallantoic membrane model (CAM) as well as within a subcutaneous murine model, with prominent angiogenesis observed within the implanted scaffolds [26,27]. The promotion of angiogenesis using only synthetic biomaterials is a challenging, yet essential requirement for a successful transplant. The current work demonstrates identification of novel synthetic, polymer-based 3D scaffolds that support growth and proliferation of FBMSCs, indicate preliminary vasculature formation and prove the significance of the innovative technique detailed herein for rapid 3D polymer scaffold formation and high throughput analysis (Fig. 1).

2. Results

2.1. Fabrication of a library of 3D polymer scaffolds and characterization

Polymer scaffolds based on 6 core acrylate polymers (polymers 1 to 6), with the potential to control stem cell fate and 3D structure [4,19], were fabricated and analysed for requisite physical properties. Arrays of 3D porous scaffolds were generated using various polymerization mixtures (Table 1) with different levels of porogens in flat-bottomed polypropylene 96-well plates. Low temperatures were used to drive phase separation between the porogen and the polymerization mixtures with UV photo-polymerization used to cure the monomers, resulting in porous polymeric materials [19]. From the perspective of the required mechanical properties and 3D microstructures, the polymeric scaffolds used a polymer composition that resulted in a stiff substrate and an interconnected porous structure with pores ranging from 100 to 400 μm.

Analysis of scaffold microstructure was carried out using micro-computed tomography (micro-CT) adapted to allow characterization of twelve 3D polymer scaffolds in a single scan. Representative transverse images of the "high" porosity scaffolds (HPS (80 % *v*/v DMSO)), the "medium" porosity scaffolds (MPS (60 % *v*/v DMSO)), together with their non-porous controls (CPS (0 % v/v DMSO)) of polymers 1 to 6 illustrate the increase in porosity and pore size with porogen levels (Fig. 2).

Images of the transverse section of 2-HPS (polymer 2 with high porosity) showed a highly interconnected porous structure with pore channels penetrating into the scaffolds (Fig. 3A). In contrast, scaffolds with medium porosity displayed denser packaged structures.

Interestingly, both scaffolds of polymer 2 with "medium" and "high" porosity displayed high density connectivity as quantified using the BoneJ plugin in ImageJ (Fig. S1) [28]. The porosity of the polymer scaffolds was tuned effectively by the level of DMSO in the polymerization mixture (Fig. 3B)' while analysis using 3D distance modelling demonstrated highly abundant pores independent of the scaffold composition and, on average, larger than 100 μm for MPS and HPS (Fig. 3C). Analysis of the pore size distribution showed the presence of pores larger than 200 μm for scaffolds generated using polymers 1, 2 and 5 (Fig. S2).

Indentation moduli (stiffness) of the scaffolds were calculated using a linear model for semi-infinite media (ratio sample area to indenter diameter ≥ 3) previously described using flat indenters (Fig. S3, Fig. 3D) [29–31]. HPS of polymers 1, 2 and 5 showed no significant differences amongst the scaffolds, whereas 1-HPS was observed to produce stiffer materials than HPS of polymers 3, 4 and 6 ($p \leq 0.001$). Indentation moduli for 2-HPS and 3-HPS were shown to be 3.1 MPa and 22.0 kPa respectively, which confirmed that polymer composition can modulate and tune the scaffold mechanical properties. Stress relaxation or relaxation load, the ability to withstand loads without breaking [32,33], were determined after 5 min relaxation to allow the scaffolds to reach equilibrium [34,35]. Relaxation load of the porous polymer scaffolds were

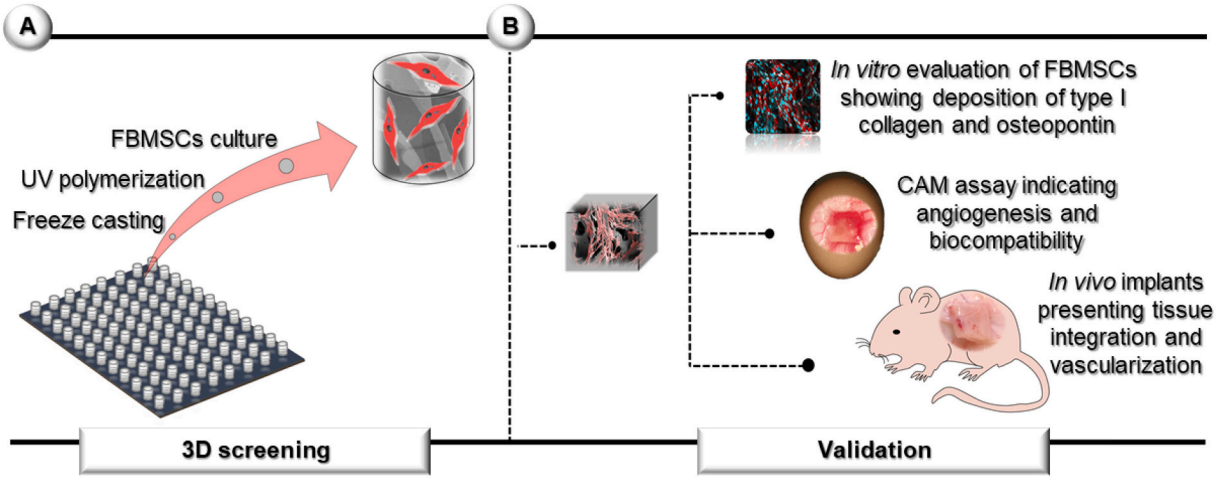

Fig. 1. (A) Screening and validation strategy for the identification of functional 3D porous scaffolds that promote the formation of vascularized tissue *in vivo*. Arrays of 3D porous scaffolds containing FBMSCs were used to rapidly analyse and identify optimal polymer compositions and 3D structures. (B) Selected scaffolds with relevant physical properties and *in vitro* cell behaviour were scaled-up to study scaffold biocompatibility and angiogenesis, *in vitro* production of ECM and *in vivo* tissue formation with vascularization.

Table 1
Polymer composition for the fabrication of the 3D porous scaffold arrays. The polymerization mixtures contained the photo-initiator (10 % mol), the cross-linker (18 % mol) and the monomers (72 % mol). DMSO was used as solvent to obtain porous scaffolds of medium porosity (MPS) (60 % *v*/v DMSO) and high porosity (HPS) (80 % v/v DMSO) together with their non-porous controls CPS (0 % v/v DMSO). Full chemical name list for each monomer can be found in Table 2.

Code	Polymer composition		Ratio (mol %)	
	M (1)	M (2)	M (1)	M (2)
1	IBA	–	72	–
2	MTEMA	IBA	36	36
3	MTEMA	EGDPEA	36	36
4	BMA	BHA	36	36
5	BMA	IBA	36	36
6	BMA	EGDPEA	36	36

governed by scaffold composition and 3D structure (Fig. S4). Overall, the porous scaffolds displayed greater relaxation (>20 %) in comparison to scaffolds devoid of pores. Interestingly, the HPS and MPS scaffolds displayed comparable mechanical properties to collagenous bone, articular cartilage and trabecular bone [36–40].

2.2. Screening of 3D porous scaffolds with FBMSCs for in vitro tissue formation

FBMSC proliferation, high collagen deposition and rapid increases in ALP in the absence of supplemented medium were used as markers to identify optimal polymer composition and 3D structures.

The proliferation of FBMSCs on the array of 3D polymer scaffolds was quantified over 21 days using resazurin (also known as Almar Blue or alamarBlue™) (Fig. S5). A rapid increase in the number of cells was observed on the majority of the 3D scaffolds, between days 0 and 2 (Fig. S6). This was followed by a stationary phase (plateau) in cell proliferation, between days 2 and 21, observed on scaffolds with no pores and scaffolds of medium porosity. In contrast, FBMSCs in polymers containing larger levels of porosity showed slightly reduced numbers of FBMSCs (Fig. 4A). The effect of the 3D scaffolds on collagen deposition was quantified using the Pico-Sirius red assay [41,42]. Increased collagen secreted by the FBMSCs at day 21 was observed in the porous scaffolds (MPS and HPS), compared to the non-porous scaffolds and the TC control (Fig. S7, Fig. 4B), indicating the formation of ECM promoted by FBMSCs within a 3D microenvironment [43,44]. Alkaline phosphatase expression, an early osteoblast differentiation marker, was assessed at days 2, 7 and 21 across all scaffolds and normalized to total DNA content and ALP expression in the control tissue culture (TC) well plate [45,46]. The majority of the polymer scaffolds expressed greater ALP than the control samples without pores (Fig. S8, Fig. 4C) at day 7, with up to a 4-fold increase observed in the case of 3-HPS ($p \leq 0.001$). A reduction in ALP was subsequently observed at day 21, across all conditions (scaffolds and control), with the exception of 4-HPS constructs that displayed a 4-fold increase in ALP. The results observed, demonstrate that differentiation of FBMSCs towards the osteogenic lineage was prominent during the early stages of culture (7 days), followed by the presentation of an enhanced differentiated phenotype with a decrease of ALP at day 21.

FBMSCs behaviour and physical characteristics of the scaffolds were used to identify an optimal porous scaffold (Fig. S9). 2-HPS and 3-HPS were shown as two strong candidates (Fig. 4D). 2-HPS provided a significantly stiffer substrate with slightly larger porosity and pore size than 3-HPS. Moreover, FBMSCs proliferation on 2-HPS was enhanced on 3-HPS with comparable collagen deposition. In marked contrast, 3-HPS was observed to promote a rapid increase in collagen and ALP, indicating the potential of the scaffold to promote FBMSCs production of bone ECM (Fig. S10). Scaffolds composed polymer 1, 4, 5 and 6 failed to display comparable osteogenic activity.

Immunofluorescence ALP staining was used to validate the screening approach applied to the array of 3D polymer scaffolds (Fig. 4E). Quantification of FBMSCs showed an ~5-fold increase in cell numbers between day 2 and 7 (comparable to the Alamar Blue data) together with a decrease in ALP expression, indicating progression towards a more differentiated osteoblast phenotype (Fig. S11). Moreover, SEM images of FBMSCs laden scaffolds demonstrated a layer of cells across the surface and the intra-porous sections, forming 3D cellular arrangements (Fig. S12). The highly porous scaffold, 2-HPS, was noted to be completely covered with FBMSCs following culture (Fig. 4F).

2.3. Angiogenesis evaluation and biocompatibility

The chick chorioallantoic membrane (CAM) model was used to provide further insights on the biocompatibility and angiogenic potential of the select polymer scaffolds [47,48]. Angiogenesis in 2-HPS and 3-HPS FBMSCs seeded scaffolds was examined following implantation in day-10 staged CAM eggs. Blood vessel integration was quantified using Chalkley scores after 7 days post-implantation. Chick eggs subject to the

Table 2
Key source table.

Reagent or resource	Source	Identifier
Chemicals		
2-(Methylthio)ethyl methacrylate (MTEMA)	Sigma-Aldrich	CAS# 14216–23-0; Cat# 423335
Butyl methacrylate (BMA)	Sigma-Aldrich	CAS# 5888-33-5; Cat# 235865
Isobornyl acrylate (IBA)	Sigma-Aldrich	CAS# 97–88-1; Cat# 392103
Ethylene glycol dicyclopentenyl ether acrylate (EGDPEA)	Sigma-Aldrich	CAS# 65983–31-5; Cat# 407968
1,6-Hexanediol diacrylate (HDOBA)	Sigma-Aldrich	CAS# 13048–33-4; Cat# 246816
2-Hydroxy-2-methylpropiophenone (PI)	Sigma-Aldrich	CAS# 7473-98-5; Cat# 405655
Pepsin	Sigma-Aldrich	CAS# 9001-75-6; Cat# P7000
Sirius red S	Sigma-Aldrich	CAS# 2610-10-8; Cat# 365548
Picric acid solution	Sigma-Aldrich	CAS# 88–89-1; Cat# P6744
Phosphatase substrate	Sigma-Aldrich	Cat# P4744
1.5 M Alkaline buffer solution	Sigma-Aldrich	Cat#A9226
Cellytic M, Igepal CA-630	Sigma-Aldrich	Cat# I8896
p-Nitrophenol	Sigma-Aldrich	Cat# N7660
Dexamethasone	Sigma-Aldrich	Cat# D4902
β-Glycerophosphate disodium salt hydrate	Sigma-Aldrich	Cat# G9422
2-Phospho-L-ascorbic acid disodium	Sigma-Aldrich	CAS# 66170–10-3; Cat# 49752
4-tert-Butylcyclohexyl acrylate (BHA)	TCI	CAS# 84100–23-2
Alpha MEM eagle with UGln1 and nucleo	Lonza	Cat# BE02-002F
penicillin/streptomycin/ fungizone 10 K/10 K/25 μg	Lonza	Cat# 17-745E
Fetal bovine serum	Life Technologies	
Quant-iT™ PicoGreen™ dsDNA assay	Life Technologies	Cat# P7589
AlamarBlue™	Thermo Scientific	Cat# Y00–025
Herring sperm DNA	Promega	Cat# D1811
Vitamin D_3	Cayman	CAS# 32222–06-3; Cat# 71820
Antibodies		
Anti-Alkaline Phosphatase	Abcam	Cat# ab95462
Tissue Non-Specific antibody	Abcam	Cat# ab65834
Anti-Osteopontin antibody	Abcam	Cat# ab8448
Anti-Collagen I antibody	Abcam	Cat# ab34710
Goat Anti-Rabbit IgG (Alexa Fluor® 647)	Abcam	Cat# ab150079
Biological samples		
Human FBMSCs	Bone and Joint Research Group, University of Southampton	Southampton & South West Hampshire Local Research Ethics Committee (LREC296/100). License (PPL 30/2762)
Software and algorithms		
GraphPad Prism 5.04	GraphPad	https://www.graphpad.com/scientific-software/prism/
Imaris	Oxford Instruments IMARIS	https://imaris.oxinst.com/
Bluehill 3	Instron	https://www.instron.com/en-gb/products/materials-testing-software
QuPath	Quantitative Pathology & Bioimage Analysis	https://qupath.github.io/
ImageJ/Fiji	Fiji	https://fiji.sc/
Bonej	Bonej	https://bonej.org/

same procedure without the implanted scaffolds served as controls. The CAM assays revealed that 2-HPS with FBMSCs displayed the highest level of angiogenesis although this did not reach statistical significance compared to other groups except for the empty control (Fig. 5A). Histological analysis confirmed angiogenesis evidenced by the presence of erythrocytes and avian cells promoted due to the enhanced pore size and interconnectivity within the scaffold (Fig. S13).

Promising results from the CAM assay and the physical properties of the scaffolds justified the evaluation of *in vitro* bone markers, which provided evidence of scaffold potential for bone repair applications. *In vitro* ECM deposition by FBMSCs was determined on scaffold 2-HPS as this scaffold provided the highest angiogenic potential. FBMSCs seeded on 2-HPS scaffold were evaluated after 7 and 21 days of culture in basal and osteogenic (supplemented with calcitriol and vitamin C) media [49,50]. Enhanced type I collagen expression, over 7 to 21 days, was evident from FBMSCs staining on 2-HPS scaffolds (Fig. 5B) maintained in basal and osteogenic media (Fig. S14). Type I collagen deposition on 2-HPS scaffolds was quantified by an ELISA (Table S3). Control cultures displayed negligible collagen production with levels below the assay detection limit (data not shown), confirming ECM production was significantly improved by the scaffold composition and 3D structure. Osteopontin expression was observed to be reduced on scaffold 2-HPS whereas expression was maintained on the 2D controls, which could indicate downstream progression of the cells in terms of osteoblastic differentiation [51]. Interestingly, aggregates of FBMSCs on 2-HPS were observed at days 7 and 21 in basal and osteogenic media (Fig. 5B), while this aggregation of FBMSCs was not observed in the control. Live/dead assay confirmed viable cells were attached to the polymer (Fig. S15).

2.4. Subcutaneous scaffold implantation to assess vascular infiltration in vivo

In vivo analysis using a subcutaneous murine model was undertaken to further investigate the angiogenic properties of 2-HPS seeded with FBMSCs pre-conditioned in basal and osteogenic media [52]. The 2-HPS scaffold was selected given the enhanced long-term cell survival, proliferation and *ex-vivo* biological function observed. Morphological analysis of the scaffolds showed extensive levels of integration with the scaffolds, almost indistinguishable from the surrounding tissue, 4 weeks post-implantation (Fig. 6, top row). Histological analysis, using Alcian Blue/Sirius Red and Goldner's Trichrome, evidenced collagen staining around and within the scaffolds, on scaffold 2-HPS seeded with FBMSCs and conditioned in basal and osteogenic media displaying elevated levels of staining (Fig. 6, top and middle rows) compared to the scaffolds cultured in the absence of cells (Fig. 6, bottom row). 2-HPS scaffolds seeded with FBMSCs and maintained under osteogenic conditions showed preliminary signs of blood vessel formation within the scaffolds (Fig. 6, middle row, blue arrows). Since blood vessel formation is not typically observed in the absence of exogenously supplied growth factors or endothelial cells [16], this vasculature augurs well for the development of a new class of synthetic angiogenic materials.

The histopathological analysis of the scaffolds using H&E staining confirmed the presence of lumen-like structures together with infiltration of the scaffolds by murine cells (a property governed by the physiochemical nature of the biomaterial) evident by the presence of cells in 2-HPS without FBMSCs (Fig. 7A). Further, the presence of multinucleated giant cells (yellow arrowhead) was observed in the scaffolds, cells known to be involved in the vascularisation process [53,54]. Moreover, RBCs (red blood cells) were observed predominantly inside the blood vessel lumens in 2-HPS (with and without cell seeding) by H&E staining as a result of vascularisation. The infiltration of host cells throughout the scaffolds, including the centre of the constructs, supported the extensive vascularisation and interconnectivity of the scaffolds. To confirm angiogenesis within these implants, VEGFR-2 (vascular endothelial growth factor receptor-2) expression was probed using immunohistochemistry and was shown to be expressed predominantly at scaffold

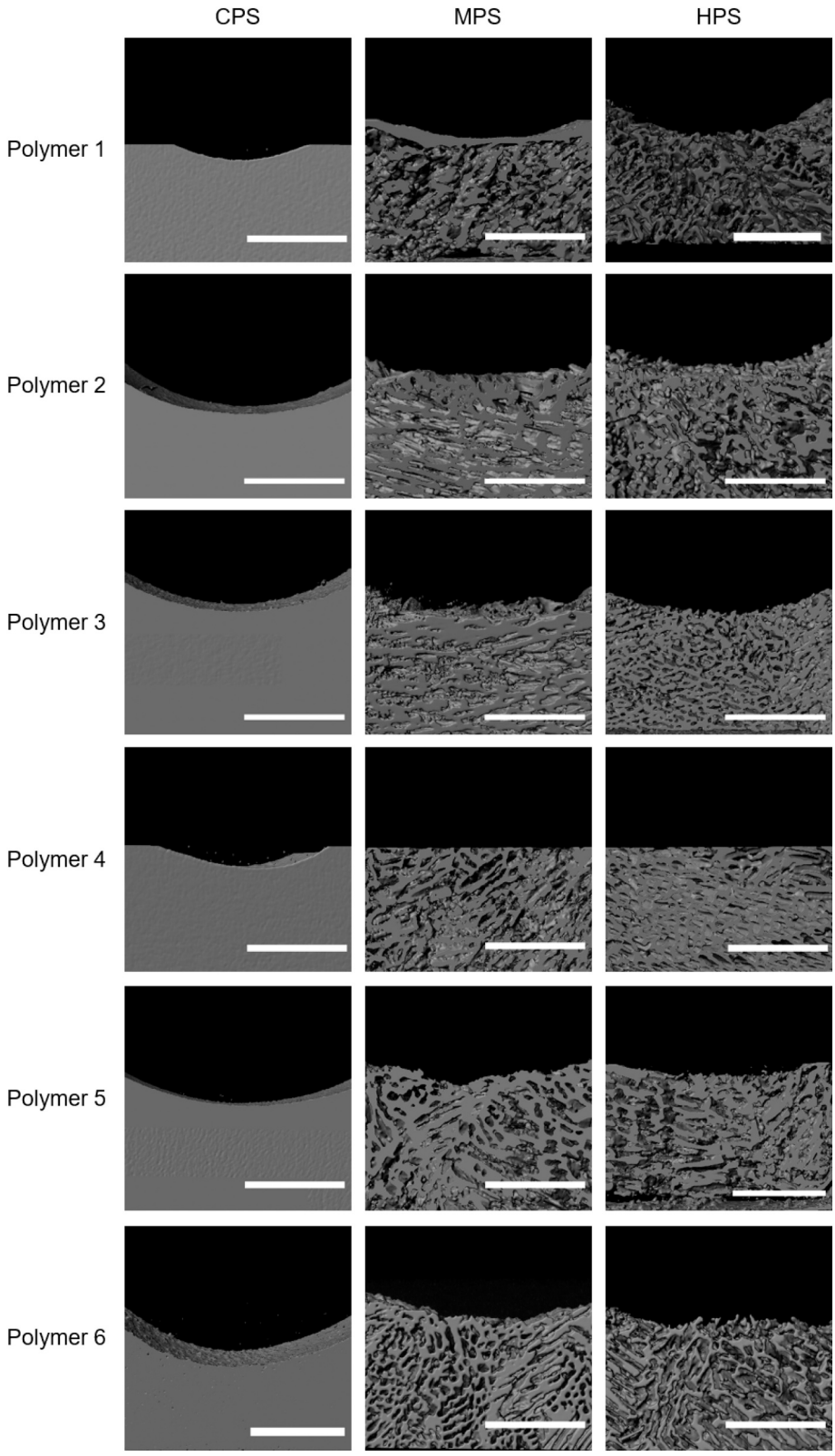

Fig. 2. Images of the 3D porous scaffolds. Longitudinal sections constructed using micro-CT data. Array of 3D porous scaffolds with scaffolds of high and medium porosity (HPS and MPS) and their non-porous controls (CPS) for polymers 1 to 6. Scale bar 1.5 mm.

boundaries and within the connective tissue (Fig. 7A). VEGFR-2 was markedly reduced in unseeded 2-HPS scaffolds. These results indicate 2-HPS pre-seeded with FBMSCs play a role in the recruitment of endothelial cells and RBCs, enhancing angiogenesis. This is in agreement with an earlier report whereby enhanced scaffold vascularisation was observed in the presence of pre-cultured osteoblasts [53]. Lumen-like structures were quantified with 2-HPS with FBMSCs conditioned in osteogenic medium displayed a significant increase in vasculature,

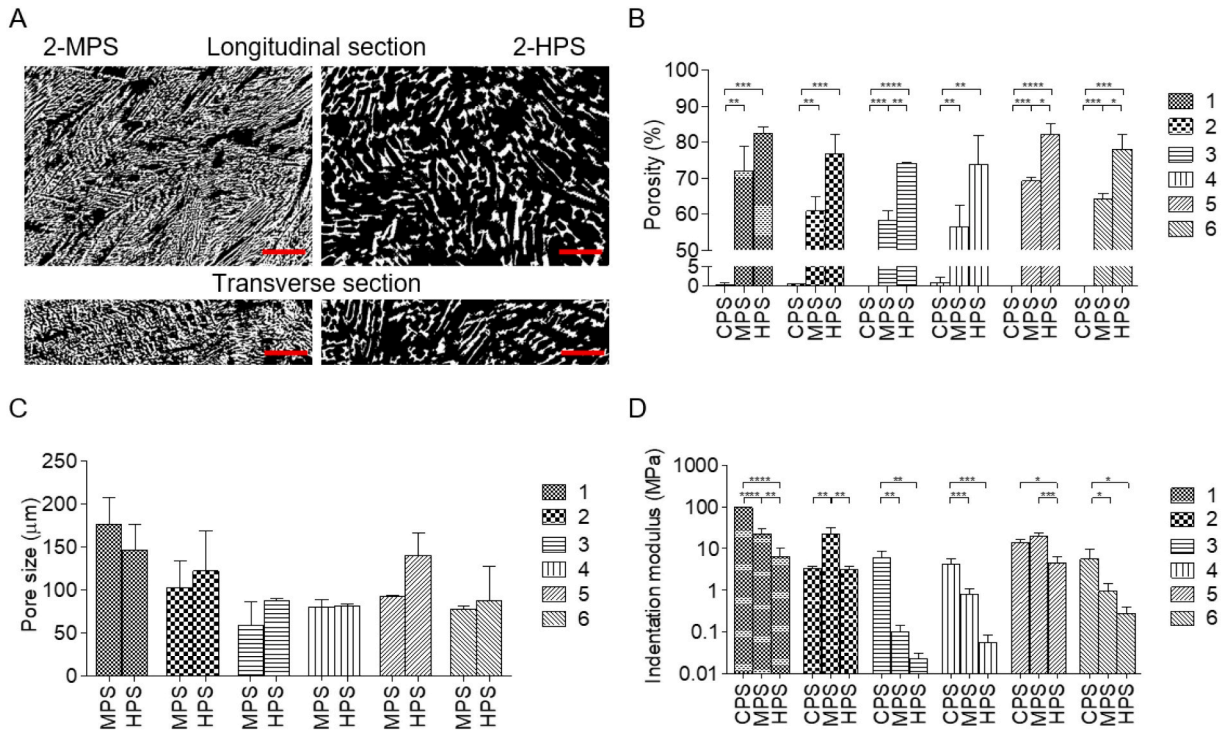

Fig. 3. Morphological and mechanical characterization of the polymer scaffolds 1 to 6. Micro-CT analysis. A) Binary images (white: polymer and black: pores) of the longitudinal and transverse sections for representative scaffolds 2-MPS and 2-HPS (scale bar 1.0 mm). B) Scaffold porosity (%) and C) 3D pore size (μm) modelled and calculated with computed spheres that fitted the pores (using ImageJ – BoneJ, two samples). Mechanical properties of the scaffolds (12 mm × 12 mm × 2 mm) were measured with a macro-indentation approach for a strain range between 5 %–10 %. D) Indentation moduli (MPa) was calculated locally (5 to 10 % strain) using a linear model for semi-infinite media from the gradient of the load *vs* displacement curves. One-way ANOVA with Bonferroni post-test (* $p \leq 0.05$, ** $p \leq 0.01$, *** $p \leq 0.001$ and **** $p \leq 0.0001$). Mean ± SD, $n = 4$.

viewed in terms of increase in the number of blood vessels lumens (identified by the presence of lumens encircled by endothelial-like cells), compared to scaffolds without cells (Fig. 7B) [55,56].

3. Discussion

3D printing offers a powerful method to generate 3D scaffolds, although, these strategies can have limited throughputs restricting their applicability in the discovery of new biomaterials [57]. Here we present highly functional 3D scaffolds, with an indication of a preliminary vasculature formation, designed by exploiting a new approach to the fabrication of scaffold libraries by varying monomer composition and porosities *via* freeze-casting and UV photopolymerization [19]. The approach allowed the rapid fabrication of a large number of scaffolds, with the 3D structures of the scaffolds controlled by modifying the level of the porogenic solvent to provide highly interconnected porous materials with potential application in skeletal tissue repair.

Tissue regeneration is critically dependent on an appropriate vascularisation that allows the necessary influx of growth factors, nutrients as well as immune cells to the area of damage to initiate the process of repair [58–60]. The ability to stimulate the process of angiogenesis (blood vessel formation) is therefore important when designing scaffolds for bone repair. For such scaffolds, variables to consider include: the material used, the cells, pre-treatment of cells and the structure of the scaffolds [61]. Synthetic polymers offer a scalable means for highly reproducible and versatile production [62]. This study set out to further characterize potential candidates from previous work by Conde-González [19] through analysis of cell compatibility and evaluation of the potential of the synthetic polymer scaffolds for bone repair [4]. Although traditional polymer microarrays allows the screening of thousands of different materials, these materials typically lack the three-dimensional organization present in tissue. The mimicry of the material 3D structure to that of the target tissue, enables evaluation and enhanced understanding of the behaviour of the material and the cells seeded upon that material to the host target tissue.

Given the scaffolds exhibited bone-like mechanical properties [63], we explored the biological properties of the scaffolds (Fig. 4) using human fetal bone marrow stromal cells (FBMSCs), due to their high proliferation rates and ability to differentiate into bone-forming cells instead of previously used osteosarcoma cell line SAOS-2 [19]. FBMSCs represent a biologically relevant target for use in skeletal tissue biofabrication. Elevated cell proliferation rates were observed together with enhanced expression of collagen and ALP on two highly porous scaffolds 2-HPS and 3-HPS high-lighting these materials as potential candidates for skeletal tissue repair applications (2-HPS is poly ($MTEMA_{36}$-*co*-IBA_{36}-*co*-$HDOBA_{18}$) with 80 % porosity and 3-HPS is poly ($MTEMA_{36}$-*co*-$EGDPEA_{36}$-*co*-$HDOBA_{18}$) with 80 % porosity).

Scaffold 2 is comprised of 2-(methylthio)ethyl methacrylate, isobornyl acrylate and 1,6-hexanediol diacrylate and scaffold 3 is comprised of 2-(methylthio)ethyl methacrylate, ethylene glycol dicyclopentenyl ether acrylate and 1,6-hexanediol diacrylate. These monomers were originally identified by Hansen et al. [4] as materials that control the growth of human embryonic stem cells (hESCs) with 2-(methylthio)ethyl methacrylate, isobornyl acrylate and ethylene glycol dicyclopentenyl ether acrylate a subgroup of monomers with high stem cell attachment properties [4]. Therefore, these materials presented themselves as candidates for the evaluation of FBMSCs attachment and proliferation. Moreover, the differences in composition between these scaffolds resulted in differences in the mechanical properties of the scaffold that were observed to modulate cell behaviour. Thus, 3-HPS was found to be a softer scaffold than 2-HPS (Fig. 3D) with accompanying biological actions/reactions. The mechanical differences resulted in the regulation of ALP and collagen levels [64], promoting FBMSCs towards a more differentiated osteoblast phenotype [65]. Our findings also

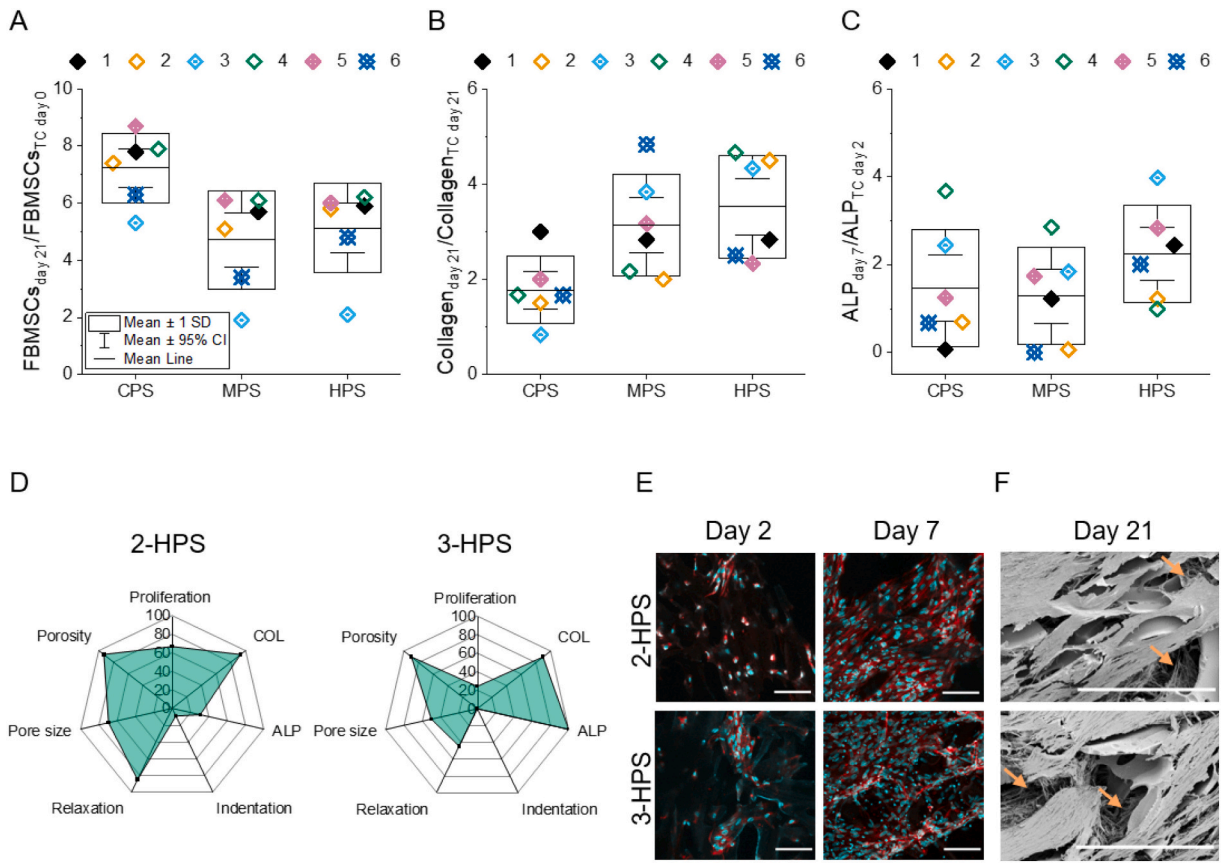

Fig. 4. Proliferation of FBMSCs and functional analysis of the 3D porous scaffolds 1 to 6 seeded with FBMSCs compared to tissue culture plate controls. A) FBMSCs proliferation on polymer 3D arrays. Cells were cultured in basal medium. Fold change of fluorescence between day 0 (10,000 cells/well) and scaffolds at day 21 (n = 3 biological replicates with 4 technical replicates). B) FBMSCs total collagen deposition on the 3D polymer arrays. Fold change of absorbance (picro-sirius red staining of collagen) between the TC control and the 3D polymer scaffolds after 21 days of incubation (n = 3 biological samples with 4 technical replicates). Cells were cultured in basal medium. C) FBMSCs alkaline phosphatase (ALP) activity within 3D polymer arrays. Fold change of absorbance (chromogenic enzymatic cleavage of phosphatase substrate) between the TC control at day 2 and scaffolds at day 21 (n = 2 biological samples with 4 technical replicates). Cells were cultured in basal medium. D) Analysis of scaffold properties and FBMSCs behaviour. FBMSCs behaviour on polymer 2 and 3 HPS scaffolds (proliferation rate at day 21, total collagen at day 21 and alkaline phosphatase at day 7) were compared with mechanical properties (indentation modulus and relaxation load) along with scaffold pore size and porosity. Each property interrogated was normalized (%) with the highest value identified (Table S2). E) Representative images of ALP expression of FBMSCs on 2-HPS and 3-HPS after 2 and 7 days of incubation in basal medium. Cell nuclei (cyan) and ALP (red). Scale bar 100 μm. F) Representative SEM images of FBMSCs within 2-HPS and 3-HPS after 21 days incubation in basal medium. Arrows show cells infiltrating throughout the scaffold. Scale bar 400 μm. (For interpretation of the references to colour in this figure legend, the reader is referred to the web version of this article.)

demonstrated enhancement of FBMSCs proliferation on stiffer materials such as tissue plastic and CPS in comparison to softer MPS and HPS materials independent of the polymer composition and porosity (Fig. S6), as previously observed by Gerardo [66].

The discovery of these high porosity scaffolds closely aligns with the observation that mesenchymal stromal cells and endothelial cells require between 100 and 400 μm pore sizes (similar pore size as in trabecular bone) for expansion, proliferation, cell-cell interactions and for facilitation of blood vessel penetration [13–15]. We previously demonstrated that the open porosity (pores connected to the surface of the scaffold) was crucial for appropriate cell penetration [19], thus reinforcing the current findings [67]. Mechanical analysis showed that the indentation properties of these materials ranged from 10 KPa to 10 MPa with a high capacity for load reduction, generating scaffold candidates for bone repair given their tuneable mechanical properties.

The chorioallantoic membrane assay provides a method to investigate the ability of a material to induce vasculature formation in an *ex vivo* model within a limited timeframe. The assay utilises implantation of a material on the extraembryonic membrane of the developing chick egg [27]. The biocompatibility of 2-HPS and, more importantly, significant angiogenesis in the absence of growth factor stimulation was evidenced using the CAM assay in contrast to 3-HPS and control scaffolds (Fig. 5A). The presence of erythrocytes and budding vasculature within the scaffolds indicated that the porosity of the material facilitated cell invasion and the formation of blood vessels. These findings suggest 2-HPS as a potential candidate for bone repair applications which will warrant further evaluation in the future (Fig. 5B) [47,48]. Preliminary *in vivo* analysis of 2-HPS scaffolds using the subcutaneous murine model demonstrated scaffold integration into murine tissue and the stimulation of vascularisation (Fig. 6). Moulisová et al. reported previously that poly (ethyl acrylate) was capable of triggering spontaneous formation of fibronectin, which in turn caused recruitment of VEGF [68,69], thus explaining the spontaneous vasculature formation within the novel poly-acrylate blends used in this study. Furthermore, the presence of multinucleated giant cells and VEGF expressed by the invading cells within the scaffolds (Fig. 7), highlights the stimulatory effect on angiogenesis from the scaffold. The most significant vasculature formation was observed in scaffolds seeded with FBMSCs conditioned in osteogenic medium evidenced by an increase in the number of blood vessels lumens (identified by presence of lumen encircled by endothelial-like cells), compared to scaffolds without cells [55]. This is in agreement with an earlier report whereby enhanced scaffold vascularisation was observed in the presence of pre-cultured osteoblasts [53].

The novel, high throughput technique developed and published

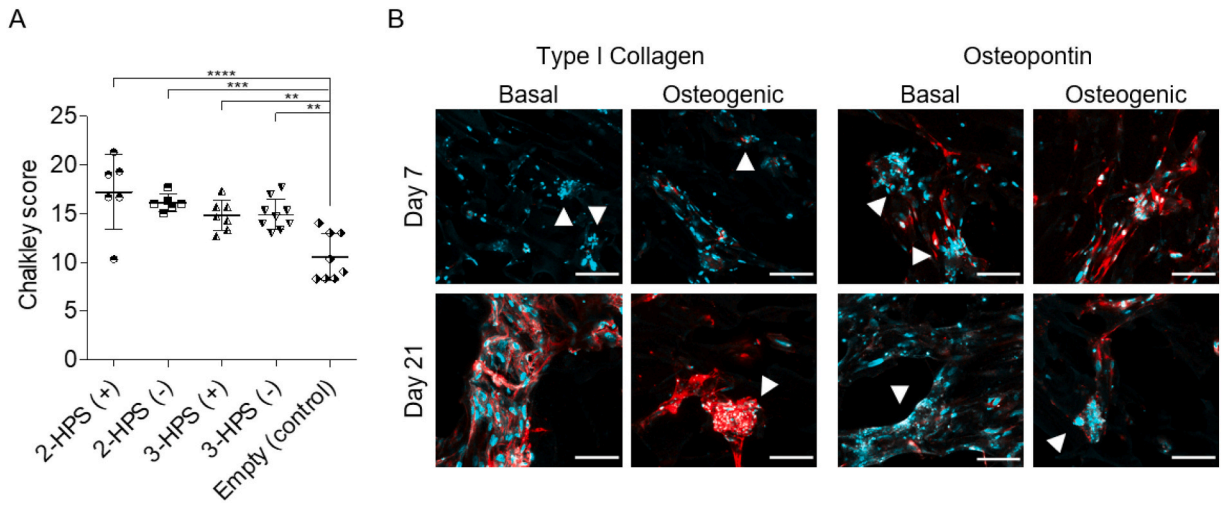

Fig. 5. Evaluation of biocompatibility. A) Chick CAM *ex vivo* model implantation of scaffolds 2-HPS and 3-HPS with (+) and without (−) FBMSCs after basal conditioning. Quantification of the vasculature *via* Chalkley score of chick CAM. Sham operated chick eggs, with an opening created in the eggshell and in the absence of implanted scaffolds served as controls (empty). One-way ANOVA with Bonferroni post-test (* $p \leq 0.05$, ** $p \leq 0.01$, *** $p \leq 0.001$ and **** $p \leq 0.0001$). Mean ± SD, $n = 5$–9. B) *In vitro* evaluation of FBMSCs production of bone ECM on 3D porous polymer scaffolds. Scaffolds 2-HPS were seeded with FBMSCs and cultured in basal and osteogenic media for 7 and 21 days. Immunofluorescence assessment for expression of type I collagen (stained red) and osteopontin (stained red) together with DAPI nuclear staining (stained cyan). Arrows show cell aggregations. Scale bar 100 μm. (For interpretation of the references to colour in this figure legend, the reader is referred to the web version of this article.)

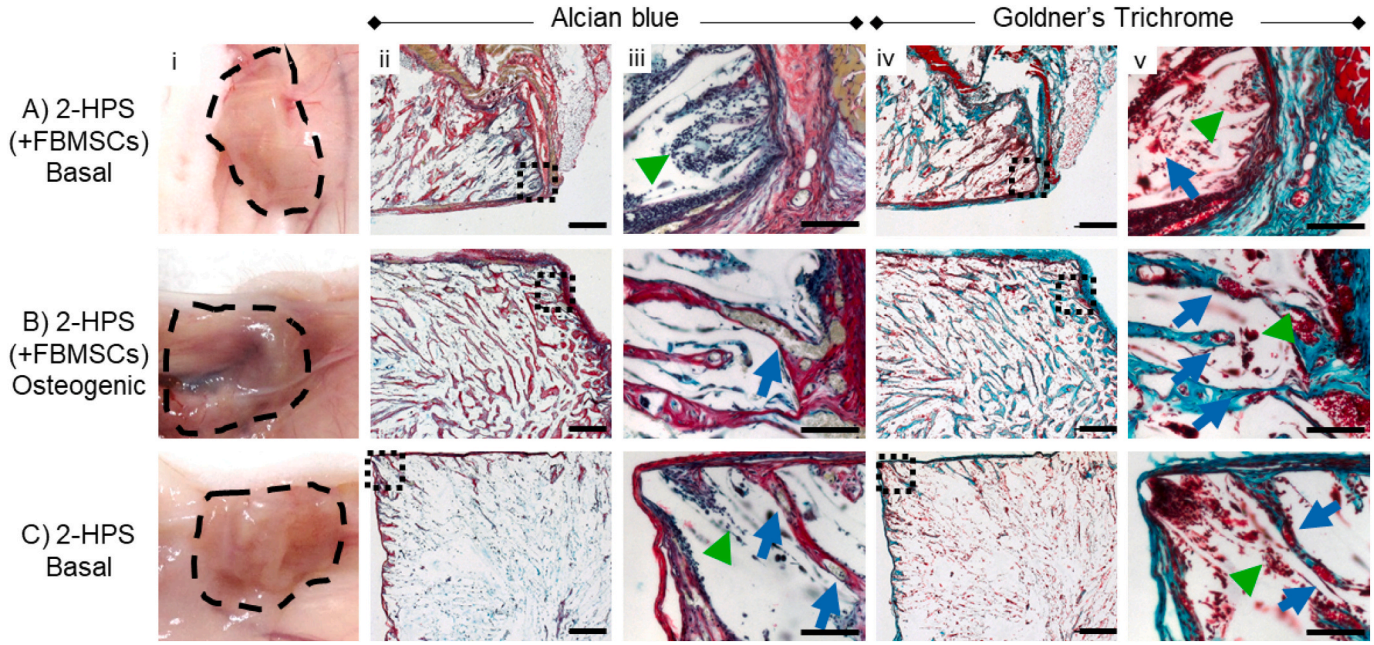

Fig. 6. Histological evaluation of 2-HPS integration, vasculature and bone formation following *in vivo* subcutaneous implantation. Macrographs of scaffold integration (i) and histological analysis with Alcian blue (ii - iii) and Goldner's Trichrome (iv-v) of 2-HPS with FBMSCs after basal conditioning (A), 2-HPS with osteogenic conditioning (B) and 2-HPS without any cells (C) showed vasculature formation throughout the scaffolds and collagen deposition after 4 weeks post-implantation. Squares show magnified areas, green arrowheads and blue arrows indicate cells and vasculature respectively. Scale bar in (ii) and (iv) 500 μm, (iii) and (v) 100 μm. (For interpretation of the references to colour in this figure legend, the reader is referred to the web version of this article.)

earlier by Conde-González et al. [19] allowed for the identification of a number of potential candidates for further analysis for biological application. The developed polymer scaffold, 2-HPS, provides a number of unique properties including: (i) promotion of host cell attraction and invasion into the scaffolds, (ii) initiation of angiogenesis and, (iii) facilitation of tissue integration and thus providing an innovative and excellent polymer scaffold candidate for further evaluation for bone repair application [70,71].

4. Conclusion

The previously developed method of high throughput screening was investigated with the use of a more targeted cell line with tissue regeneration as the endpoint. In the current studies, a new class of tissue-compatible and pro-angiogenic materials have been identified building on a previously developed 3D polymer array screening platform. The highly porous synthetic materials support and promote vascularisation upon implantation, an important requirement for tissue regeneration

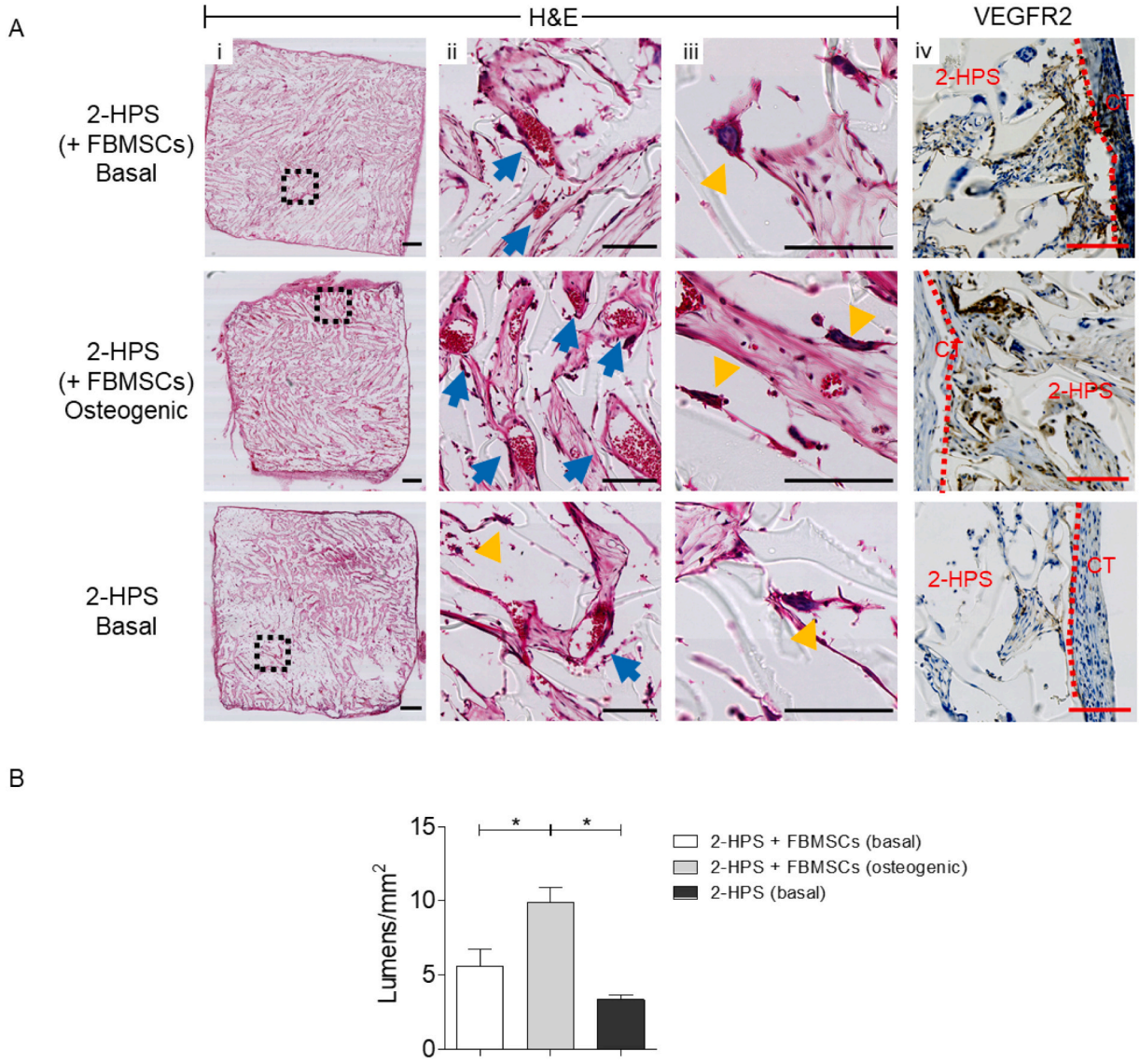

Fig. 7. A) Histological evaluation of 2-HPS scaffolds by H&E and immunohistochemistry for VEGFR-2 (vascular endothelial growth factor receptor-2). Histological analysis with H&E (i - iii) and immunohistochemistry for VEGFR-2 (iv) of 2-HPS with FBMSCs after basal conditioning, 2-HPS with osteogenic conditioning and 2-HPS without any cells showed infiltration of the scaffolds with RBCs and multinucleated giant cells. The expression of VEGFR-2 evident as a brown stain within scaffolds 4 weeks post-implantation. Squares show magnified areas, blue arrows and yellow arrowheads indicate RBCs and multinucleated giant cells. Dashed lines indicate interface between connective tissue (CT) and scaffolds. Scale bar in (i) 500 μm and (i-v) 100 μm. B) Evaluation of the number of lumens/vascular structures per mm^2 of scaffold 2-HPS containing FBMSCs after basal conditioning, 2-HPS with osteogenic conditioning and 2-HPS without any cells. Analysis was performed manually using the software QuPath on the histological sections stained with H&E. One-way ANOVA with Bonferroni post-test (* $p \leq 0.05$). (For interpretation of the references to colour in this figure legend, the reader is referred to the web version of this article.)

with widespread potential for applications in hard and soft skeletal tissue reparation. Future studies to confirm vasculature formation through long-term *in vivo* analysis, elucidation of the underlying mechanisms facilitating vasculature induction and investigation of the immune response to the foreign body will inform a new generation of polymers for growth factor-free angiogenesis with significant implications therein for regenerative medicine.

5. Materials and methods

5.1. Resource availability

5.1.1. Lead contact

Further information and requests for resources should be directed to the lead contacts, Richard O.C. Oreffo (Richard.Oreffo@soton.ac.uk) and Mark Bradley (Mark.Bradley@ed.ac.uk).

5.2. Materials availability

This study did not generate new unique reagents.

5.3. Method details

5.3.1. Arrays of 3D polymer scaffolds

The arrays of porous polymers were generated using UV-photopolymerization at <0 °C with various porogenic solutions (DMSO and the polymerization solutions, in polypropylene 96-well plates (80 μL well). The polymerization solutions (Table 1) consisted of acrylate monomers, the cross-linker 1,6-hexanediol diacrylate and the photoinitiator 2-hydroxy-2-methylpropiophenone. For freezing the

arrays were cooled to 5 °C for 16 h, sealed inside a polyethylene box and subsequently further cooled to −20° over 4 h. UV-polymerization (UV cross-linker CL-1000 L 8 W, 365 nm, 30 min) was accomplished on top of an aluminium cooling plate (128 × 86 × 10 mm) placed on a dry ice bath. After UV curing the arrays were washed with ethanol/water (1:1, 2 days) followed by water (2 days) at 37 °C inside an oven before freeze-drying (2 days).

5.3.2. Scale up of the 3D scaffolds

Larger porous scaffolds (12 × 12 × 2 mm) were prepared in a similar approach as above with the solutions placed inside a custom polystyrene mold (10 × 10 × 7 mm) and cooled at 5 °C for 16 h and then frozen at −20 °C for 4 h before UV-photopolymerization for 60 min. Subsequently, the scaffolds were extracted from the mold and placed in falcon tubes with water – ethanol (1:1 for 3 days) and then water (5 days) at 37 °C inside an oven before freeze-drying (3 days). The wash process resulted in a modest swelling of the scaffolds to their final size (12 × 12 × 2 mm).

5.3.3. Micro-CT morphological analysis of 3D porous scaffolds

A cuboid generated by stacking 12 different samples of 3D polymer scaffolds was arranged and scanned through 360° with a step of 0.48° between the exposures using a Skyscan 1172 desktop micro-CT (Bruker, Kontich, Belgium). Micro-CT was set up with a 34 kV source voltage, 210 μA source current and with an exposure time of 1764 ms with a resolution of 5.94 μm with 4 frames taken at each position and averaged to reduce noise. Skyscan NRecon v1.6.9 (Bruker, Kontich, Belgium) was used to reconstruct the data using a thresholding window of 0.00 to 0.05 in CT attenuation coefficient without beam hardening correction. Volumes of interests of reconstructed micro-CT scans were binarized and characteristics of the scaffolds was analysed with the ImageJ plugin BoneJ [28]. Porosity was defined as the fraction between the volume of pores and the scaffolds total volume. Pore size along with the thickness of the scaffold walls were defined as the average diameter of a theoretical sphere of the same volume to that of the volume of these constructions. 3D images of the scaffolds were constructed with the contour surface mode of Imaris.

5.4. Mechanical characterization

An Instron compression system (model 3367) equipped with the software Bluehill 3 (Norwood, USA), a flat cylindrical (diameter 1 mm) indenter (made in house) in addition to a 50 N cell were used for compression to mechanically characterize the re-hydrated 3D scaffolds (12 × 12 × 2 mm). Samples were compressed for 20 % of the strain (average height measured with Vernier calipers was about 1.7 mm) at a strain rate of 5 % per minute. Relaxation at constant stress was measured for 5 min. The indentation modulus was determined using a linear model for semi-infinite media (ratio surface of the sample to its high ≥3) previously described [30,31,72]. A linear model was applied with load-displacement curves locally between four strain regions; 0 %–5 %, 5 %–10 %, 10 %–15 % and 15 %–20 %. The relaxation load (%) was determined as the percentage reduction of load after 5 min relaxation [34,35].

5.4.1. Protocol for FBMSCs culture in the arrays and scaffolds

Human FBMSCs were provided by Dr. Stefanie Inglis and Ms. Suzanne Renz, University of Southampton. The cells were isolated as per ethical approval obtained from North East – Newcastle & North Tyneside 1 Research Ethics Committee (18/NE/0290; IRAS 250012 with thanks to Dr C Morris). FBMSCs were cultured and expanded to confluence up to passage 4 in basal culture medium (alpha-MEM supplemented with 10 % FBS and 1 % penicillin/streptomycin/fungizone) before seeding. The polymer scaffolds were sterilized under UV irradiation (overnight). In the case of the array of 3D polymer scaffolds, 96-well plates were used as molds (dimensions 6.4 mm × 5 mmm, Ø x h), cells were seeded in suspension (10,000 cells in 150 μL) and were incubated in a humidified atmosphere (37 °C and 5 % CO_2) with media changed every 2 days. Scaled up 3D scaffolds (dimensions 12 mm × 12 mm × 2 mm, L x W x h) were placed inside cell culture inserts and seeded with a suspension of cells (40,000 cells in 110 μL of basal media). FBMSCs were left for 45 min for attachment before covering with media (2 mL) which was changed every 2 days. Osteogenic differentiation media; basal media supplemented with 2-phospho-L-ascorbic acid (50 μg/mL) and calcitriol (10 nM) [73]. Mineralization media; basal media supplemented with dexamethasone (10 nM), 2-phospho-L-ascorbic acid (50 μg/mL) and β –glycerophosphate (20 mM) [45,74,75].

5.4.2. Proliferation assay with AlamarBlue™ in the array

An AlamarBlue™ assay was used to assess FBMSCs viability on the array of 3D polymer scaffolds. At the appropriate time (day 2, 7, 14 or 21), basal culture medium was removed to add 100 μL per well of AlamarBlue™ solution (10 % *v*/v) in media. Incubation was carried out in humidified atmosphere (37 °C and 5 % CO2) for 4 h before collecting the supernatant to determine fluorescence intensity (λex/em = 530/590 nm) in a microplate reader (GloMax®, Promega). The arrays were washed with PBS to remove excess of AlamarBlue™ solution and basal media added (150 μL/well) to maintain the FBMSCs in culture until the next time point.

5.4.3. Total collagen in the array

The total collagen content of the FBMSCs cultured with basal medium, in the array of 3D polymer scaffolds, was assessed using a previously published colorimetric method [41,42]. Briefly, FBMSCs on porous scaffolds following 21 days incubation were digested with pepsin (1 mg/mL pepsin, 0.1 M acetic acid and 0.5 M NaCl) for 48 h at 5 °C and 100 μL from each digested solution was dried in a 96-well plate at 37 °C overnight. Dried samples were treated with 100 μL of Sirius red solution (1 mg/mL) in saturated picric acid (1.3 % in water) for one hour before washing (3 × 5 min) the excess with HCl solution (0.1 N). 100 μL of NaOH solution (0.1 N) was used to resolve the staining and a microplate reader was used to record absorbances (λ = 550 nm).

5.4.4. ALP expression in the array

FBMSCs cultured in basal medium in the array of 3D polymer scaffolds were first washed with PBS prior to addition of CelLytic M (1 h, 37 °C) to lyse the cells. 10 μL of cell lysate was placed in a fresh 96-well plate with 90 μL of ALP substrate solution (0.04 g phosphatase substrate in 10 mL of 1.5 M alkaline buffer solution (Sigma A9226) buffer solution made up to a final volume of 30 mL with distilled H2O). Samples were incubated at 37 °C for between 10 and 60 min and the reaction was stopped by the addition of 100 μL of NaOH (1 M). A standard calibration curve (0 to 2 μM) was constructed using serial dilutions of p-nitrophenol (10 mM) in assay buffer. The assay buffer for the standards was prepared by addition of 30 μL of Igepal CA-630 to 5 mL of 1.5 M alkaline buffer solution (Sigma A9226) and made up to a final volume of 15 mL with distilled H2O. Absorbance was read on a microplate reader (λ = 410 nm) and ALP concentration calculated as nmoles of p-nitrophenol per mL/h. ALP expression was normalized to the DNA concentration using a Quant-iT™ PicoGreen™ dsDNA assay kit. A standard calibration curve (0 to 1000 ng/mL) was constructed using serial dilutions of herring sperm DNA (10 mg/mL) in TE buffer and fluorescence intensity determined using a microplate reader (λex/em = 480/520 nm).

5.4.5. Scanning electron microscopy (SEM)

FBMSCs cultured with basal medium in the 3D porous scaffolds (12 × 12 × 2 mm) were first washed with PBS (2 × 5 min) and subsequently fixed with paraformaldehyde (PFA, 4 % *w/v*) for 30 min. Excess PFA was removed with cacodylate buffer (0.1 M, 1 h) and subsequently the scaffolds were treated with osmium tetroxide (1 %, 15 min) in cacodylate buffer (0.1 M). After a further wash with cacodylate buffer (15 min) the scaffolds were dehydrated with acetone (50 %, 70 %, 90 % and 100

%) and liquid CO2 (critical point drying) before coating the samples with gold/palladium. Hitachi S-4700 scanning electron microscope was used to image the specimens.

5.4.6. Chorioallantoic membrane (CAM) assay

The CAM protocols were conducted under Home Office Approval UK (Project license — PPL 30/2762). Chicken eggs were incubated (1-h rotation) in a Hatchmaster incubator (Brinsea, UK) for 10 days at 37 °C in a 60 % humidified atmosphere. After 10 days post-fertilisation, a scalpel was used to create a 5 × 5 mm window on the eggshell under sterile conditions. The polymeric scaffolds ($n = 10$) of size (10 × 10 × 5 mm) were pre-conditioned with or without FBMSCs (40,000 cells per scaffold), which were cut into 5 × 5 × 5 mm cubes and implanted. The eggs were sealed with sterile parafilm and the eggs candled every day to inspect for embryo development. After a further 7 days of incubation in basal medium, the samples were harvested, and CAM integration inspected using a stereomicroscope with a digital camera (Canon Powershot G2). Gestational processes were terminated under specific Home Office guidelines. Chick eggs that followed the same procedure with the exception of the implantation of the scaffolds were used as controls (empty). Animal procedures were undertaken in accordance with the guidelines and regulations of the Animals Act 1986, UK.

5.4.7. Immunostaining of FBMSCs on the 3D scaffold

FBMSCs were seeded on scaled-up 3D scaffolds and maintained in basal and osteogenic media for the desired time points (days 2, 7 and 21). At the end of the culture period, the scaffolds were washed with PBS and fixed with 4 % PFA for 30 mins. Thereafter, excess fixative was removed and the cells on the scaffolds treated with the appropriate blocking solutions and permeablised as necessary (ALP: 1 % BSA + 10 % normal goat serum in 0.1 % Tween, Collagen I: 5 % BSA, Osteopontin: 1 % BSA + 10 % normal goat serum in 0.1 % Tween) for 1 h. The scaffolds were washed thoroughly with PBS followed by exposure to the appropriate primary antibody (incubation overnight), washed with PBS and treated with a secondary antibody for 1 h. Finally, the scaffolds were washed with PBS and subjected to confocal microscopy using a ZEISS LSM 880 confocal microscope.

5.4.8. Enzyme-linked immunosorbent assay (ELISA) on the 3D scaffold

FBMSCs were seeded on scaled-up 3D scaffolds and maintained for 21 days in basal medium. At the end of the culture period, the scaffolds were washed with PBS and the cells solubilized using 400 μL 1× extraction buffer. The scaffolds were crushed and the lysate was incubated in ice for 15 mins. It was then centrifuged at 15000 x*g* for 20 min at 4 °C. The supernatants were collected and passed through PierceTMProtein Concentrator PES, (30,000 K MWCO, 2-6 ml) and the samples obtained were stored at −80 °C. The total protein was quantified using BCA assay kit for low protein concentrations (ab207002). ELISA was performed using Human Pro-Collagen I SimpleStep ELISA Kit (abcam) according to manufacturer's instructions with absorbance determined at 450 nm in a microplate reader.

5.4.9. Imaging of the cell aggregates on 3D scaffold

FBMSCs were seeded on scaled-up 3D scaffolds and maintained for 21 days in basal medium. The 3D Scaffolds were washed and stained using a Live/Dead staining kit (Invitrogen) according to the manufacturer's instructions. Finally, the scaffolds were subjected to confocal microscopy using a ZEISS LSM 880 confocal microscope.

5.4.10. In vivo subcutaneous implantation in mice and analysis

The subcutaneous surgeries were conducted under Home Office Approval UK (Project license — PPL 30/2762). Balb/c nu/athymic mice were grown until 3-months old and a weight of ~33 g, before the implantation took place. The animals were anaesthetized with an intraperitoneal injection of a hypnorm-hypnovel (1:1) mix. An incision on the back of the mouse skin was made with 2–3 pockets generated for the implantation of scaffolds. The incision was then stitched, and animals allowed to recover under constant supervision. Three groups were assessed: i) samples of polymer 2 with FBMSCs conditioned in basal and osteogenic media and ii) polymer 2 without cells conditioned in basal medium. The polymeric scaffolds were cut into 5 × 5 × 5 mm cubes. The animals were scanned at weeks 2 and 4 post-surgery using micro-computed tomography (μCT) (Bruker Skyscan 1176, equipped with micro-focus X-ray source, 20–90 kV, 25 W) and terminated at week 4 for sample collection. Atotal of seven mice were used with 2/3 scaffolds per side (4/6 per mouse) to provide a total $n = 8$ scaffolds for each of 4 groups (total 36 scaffolds). Animal procedures were undertaken in accordance with the guidelines and regulations of the Animals Act 1986, UK.

5.4.11. Histology analysis

Recovered samples were fixed overnight at 4 °C (paraformaldehyde, 4 %) and then dehydrated in auto-processing machine Shandon Citadel 200 (Thermofisher, UK) for 1 h each through 50 %, 90 % and 100 % ethanol, followed by two dehydration steps in 100 % Histoclear (Fisher Scientific UK, 12624077). The dehydrated samples were then embedded in hot wax twice for 1 h each. To ensure full wax penetration into the scaffolds, the samples were further embedded under vacuum in a Vacutherm oven (Heraeus, Thermofisher, UK) for 1 h at 60 °C. Sections were cut once, at room temperature, to 7 μm on a Microm330 microtome (Optec UK) and transferred to glass slides (preheated at 37 °C for approximately 2 h). The samples were stained as previously described [8,76]. Briefly, prior to staining, the tissue slide sections were brought to room temperature and rehydrated through a series of steps: Histoclear (2 × 7 min) and decreasing ethanol solutions: 2 × in 100 % ethanol, 90 % ethanol and 50 % - all for 2 min. For Alcian Blue/Sirius Red, the Weigert's Hematoxylin (Fisher Scientific UK, 10181710) was applied for 10 min to stain the cell nuclei. Any excess stain was removed by immersing into 1 % (*v*/v) hydrochloric acid / 70 % (v/v) ethanol solution and washed in H2O. Slides were immersed in 0.5 % Alcian blue 8GX (Fisher Scientific UK, 40046–0100) in 1 % acetic acid for proteoglycan expression. Slides were treated in 1 % molybdophosphoric acid (Sigma-Aldrich UK, 221856) prior to staining with 1 % Sirius red F3B (Direct Red 80, Sigma 365,548) to collagen visualisation. For Goldner's Trichrome, the sections were stained again with Wiegert's Hematoxylin and washed in 1 % (v/v) HCl / 70 % (v/v) EtOH. The samples were then treated with Ponceau-Fuchsin and Axophloxin solutions (0.75 % (v/v) ponceau de xylidine, 0.25 % (v/v) acid fuchsin and 0.5 % (v/v) azophloxin dissolved in 1 % acetic acid solution) for muscle and cytoplasm visualisation. Slides were treated in 0.6 % (*w/v*) molybdophosphoric acid with 0.4 % (w/v) Orange G (Sigma, UK, O3756) to visualize erythrocytes. The slides were washed in 1 % acetic acid solution and stained with 0.2 (w/v) Light green SF (Sigma, UK, L5382) to visualize collagen. Any excess stain was rinsed off with H2O (for Alcian Blue/Sirius Red) or 1 % acetic acid (for Goldner's Trichrome) and slides were again dehydrated in increasing concentrations of ethanol and Histoclear, before mounting with dibutyl phthalate xylene (DPX) (Fisher Scientific UK, 10050080) and imaging on a Zeiss Axiovert200 digital imaging system. For immunohistochemistry, heat mediated antigen retrieval was undertaken for 20 min in citrate-based buffer (BOND Epitope Retrieval Solution 1, pH 6; Leica Biosystems) for detection of VEGFR-2. Following a peroxidase block for 10 min, the sections were incubated for 60 min at room temperature with VEGFR-2 antibody (Millipore 07–1294) at a 1:100 dilution. Sections were subsequently incubated with anti-rabbit horseradish-peroxidase labelled polymer for 15 min and thereafter with the diaminobenzidine for 10 min. The slides were then counterstained for 5 min with hematoxylin (BOND Polymer Refine Detection Kit; Leica Biosystems) and thereafter dehydrated, cleared and mounted. For H&E staining, samples were dewaxed and rehydrated. The samples were placed in hematoxylin for 5 min and washed in running water for 20 s. Thereafter they were differentiated in 1 % acid alcohol followed by Scott's Tap Water Substitute for 2 min. The

eosin solution was used to stain for 2 min followed by washing in running water for 20 s. The samples were then dehydrated, cleared in xylene and mounted.

5.4.12. Evaluation of the number of lumens/vascular

Lumens and vascular-like structures were evaluated using histological sections stained with H&E and the software QuPath. Lumens and vascular structures were counted manually and normalized by scaffold area.

CRediT authorship contribution statement

A.C., M.G., D.D. contributed equally carrying out the experiments. A. C.-G., M.G., D.D., R.O.C.O., M.B. wrote the manuscript. A.C. provided rheological expertise and R.W. strucutral analysis. R.O.C.O and M.B. supervised the experimental work and manuscript. All authors read and commented on the manuscript.

Declaration of competing interest

The authors declare that they have no known competing financial interests or personal relationships that could have appeared to influence the work reported in this paper.

Data availability

Data will be made available on request.

Acknowledgements

We acknowledge the European Research Council for funding (ERC-2013-ADG 340469 ADREEM), the SuRF for histological services (University of Edinburgh), Mr. Stephen Mitchell for his technical support in scanning electron microscopy (Biology Scanning EM Facility, University of Edinburgh) and Dr. Daniel Norman (University of Edinburgh). Support from the UK Regenerative Medicine Platform Hub Acellular SMART materials 3D architecture (MR/R015651/1), the UK Regenerative Medicine Platform (MR/L012626/1 Southampton Imaging), Dr. Stefanie Inglis and Dr. Suzanne Renz are also gratefully acknowledged.

Appendix A. Supplementary data

Supplementary data to this article can be found online at https://doi.org/10.1016/j.bioadv.2022.213250.

References

[1] L. Krishna, K. Dhamodaran, C. Jayadev, et al., Nanostructured scaffold as a determinant of stem cell fate, Stem Cell Res.Ther. 7 (188) (2016), https://doi.org/10.1186/s13287-016-0440-y.
[2] M. Sancho-Tello, F. Forriol, J.J. Martín de Llano, et al., Biostable scaffolds of polyacrylate polymers implanted in the articular cartilage induce hyaline-like cartilage regeneration in rabbits, Int. J. Artif. Organs 40 (7) (2017) 350–357, https://doi.org/10.5301/ijao.5000598.
[3] E. López-Ruiz, S. Venkateswaran, M. Perán, et al., Poly(ethylmethacrylate-co-diethylaminoethyl acrylate) coating improves endothelial re-population, biomechanical and anti-thrombogenic properties of decellularized carotid arteries for blood vessel replacement, Sci. Rep. 7 (1) (2017) 1–14, https://doi.org/10.1038/s41598-017-00294-6.
[4] A. Hansen, H.K. Mjoseng, R. Zhang, et al., High-density polymer microarrays: identifying synthetic polymers that control human embryonic stem cell growth, Adv.Healthc.Mater. 3 (6) (2014) 848–853, https://doi.org/10.1002/adhm.201300489.
[5] R. Zhang, H.K. Mjoseng, M.A. Hoeve, et al., A thermoresponsive and chemically defined hydrogel for long-term culture of human embryonic stem cells, Nat. Commun. 4 (2013) 1335, https://doi.org/10.1038/ncomms2341.
[6] A. Aghali, H.E. Arman, Photoencapsulated-mesenchymal stromal cells in biodegradable thiol-acrylate hydrogels enhance regeneration of craniofacial bone tissue defects, Regen. Med. 15 (9) (2020) 2115–2127, https://doi.org/10.2217/rme-2020-0061.
[7] U. Shaukat, E. Rossegger, S. Schlögl, A review of multi-material 3D printing of functional materials via vat photopolymerization, Polymers 14 (12) (2022) 2449, https://doi.org/10.3390/polym14122449.
[8] F. Khan, J.O. Smith, J.M. Kanczler, R.S. Tare, R.O.C. Oreffo, M. Bradley, Discovery and evaluation of a functional ternary polymer blend for bone repair: translation from a microarray to a clinical model, Adv. Funct. Mater. 23 (22) (2013) 2850–2862, https://doi.org/10.1002/adfm.201202710.
[9] C.E. Clarkin, L.C. Gerstenfeld, VEGF and bone cell signalling: an essential vessel for communication? Cell Biochem. Funct. 31 (1) (2013) 1–11, https://doi.org/10.1002/cbf.2911.
[10] U. Sivan, J. De Angelis, A.P. Kusumbe, Role of angiocrine signals in bone development, homeostasis and disease, Open Biol. 9 (10) (2019), 190144, https://doi.org/10.1098/rsob.190144.
[11] V. Kesireddy, F.K. Kasper, Approaches for building bioactive elements into synthetic scaffolds for bone tissue engineering, J. Mater. Chem. B 4 (42) (2016) 6773–6786, https://doi.org/10.1039/C6TB00783J.
[12] W. Liu, G. Zhang, J. Wu, et al., Insights into the angiogenic effects of nanomaterials: mechanisms involved and potential applications, J. Nanobiotechnol. 18 (1) (2020) 9, https://doi.org/10.1186/s12951-019-0570-3.
[13] J.L. Simon, S. Michna, J.A. Lewis, et al., In vivo bone response to 3D periodic hydroxyapatite scaffolds assembled by direct ink writing, J. Biomed. Mater. Res. A 83 (3) (2007) 747–758, https://doi.org/10.1002/jbm.a.
[14] F.M. Klenke, Y. Liu, H. Yuan, E.B. Hunziker, K.A. Siebenrock, W. Hofstetter, Impact of pore size on the vascularization and osseointegration of ceramic bone substitutes in vivo, J. Biomed. Mater. Res. A 85 (3) (2008) 777–786, https://doi.org/10.1002/jbm.a.31559.
[15] R.A. Perez, G. Mestres, Role of pore size and morphology in musculo-skeletal tissue regeneration, Mater. Sci. Eng. C 61 (2016) 922–939, https://doi.org/10.1016/j.msec.2015.12.087.
[16] G. Papavasiliou, M.H. Cheng, E.M. Brey, Strategies for vascularization of polymer scaffolds, J.Investig.Med. 58 (7) (2010) 838, doi: 10.231/jim.0b013e3181f18e38.
[17] H. Tian, J. Du, J. Wen, et al., Growth-factor nanocapsules that enable tunable controlled release for bone regeneration, ACS Nano 10 (8) (2016) 7362–7369, https://doi.org/10.1021/acsnano.5b07950.
[18] D.M. Gibbs, C.R. Black, G. Hulsart-Billstrom, et al., Bone induction at physiological doses of BMP through localization by clay nanoparticle gels, Biomaterials 99 (2016) 16–23, https://doi.org/10.1016/j.biomaterials.2016.05.010.
[19] A. Conde-González, D. Dutta, R. Wallace, A. Callanan, M. Bradley, Rapid fabrication and screening of tailored functional 3D biomaterials, Mater. Sci. Eng. C 2020 (108) (November 2019), 110489, https://doi.org/10.1016/j.msec.2019.110489.
[20] K. Cheng, Y. Lai, W.S. Kisaalita, Three-dimensional polymer scaffolds for high throughput cell-based assay systems, Biomaterials 29 (18) (2008) 2802–2812, https://doi.org/10.1016/j.biomaterials.2008.03.015.
[21] Y. Yang, D. Bolikal, M.L. Becker, J. Kohn, D.N. Zeiger, C.G. Simon, Combinatorial polymer scaffold libraries for screening cell-biomaterial interactions in 3D, Adv. Mater. 20 (11) (2008) 2037–2043, https://doi.org/10.1002/adma.200702088.
[22] X. Li, X. Zhang, S. Zhao, J. Wang, G. Liu, Y. Du, Micro-scaffold array chip for upgrading cell-based high-throughput drug testing to 3D using benchtop equipment, Lab Chip 14 (3) (2014) 471–481, https://doi.org/10.1039/c3lc51103k.
[23] R.A. Revia, B. Wagner, M. James, M. Zhang, High-throughput dispensing of viscous solutions for biomedical applications, Micromachines 13 (10) (2022) 1730, https://doi.org/10.3390/mi13101730.
[24] P. Xia, Y. Luo, Vascularization in tissue engineering: the architecture cues of pores in scaffolds, J. Biomed. Mater. Res. 110 (5) (2022) 1206–1214, https://doi.org/10.1002/jbm.b.34979.
[25] K. O'Donoghue, N.M. Fisk, Fetal stem cells, Best Pract. Res. Clin. Obstet. Gynaecol. 18 (6) (2004) 853–875, https://doi.org/10.1016/j.bpobgyn.2004.06.010.
[26] Z. Demcisakova, L. Luptakova, Z. Tirpakova, et al., Evaluation of angiogenesis in an acellular porous biomaterial based on polyhydroxybutyrate and chitosan using the chicken ex ovo chorioallantoic membrane model, Cancers 14 (17) (2022) 4194, https://doi.org/10.3390/cancers14174194.
[27] I. Moreno-Jiménez, G. Hulsart-Billstrom, S.A. Lanham, et al., The chorioallantoic membrane (CAM) assay for the study of human bone regeneration: a refinement animal model for tissue engineering, Sci. Rep. 6 (August) (2016) 1–12, https://doi.org/10.1038/srep32168.
[28] M. Doube, M.M. Klosowski, I. Arganda-Carreras, et al., BoneJ: free and extensible bone image analysis in ImageJ, Bone 47 (6) (2010) 1076–1079, https://doi.org/10.1016/j.bone.2010.08.023.
[29] S.P. Timoshenko, J.N. Goodier, Theory of elasticity, in: McGraw-Hill (Ed.), Theory of Elasticity, 3rd ed., 1951, pp. 1–14.
[30] V. Egorov, S. Tsyuryupa, S. Kanilo, M. Kogit, A. Sarvazyan, Soft tissue elastometer, Med. Eng. Phys. (2008), https://doi.org/10.1016/j.medengphy.2007.02.007. Published online.
[31] R.M. Delaine-Smith, S. Burney, F.R. Balkwill, M.M. Knight, Experimental validation of a flat punch indentation methodology calibrated against unconfined compression tests for determination of soft tissue biomechanics, J. Mech. Behav. Biomed. Mater. 60 (2016) 401–415, https://doi.org/10.1016/j.jmbbm.2016.02.019.
[32] S.A. Ashter, Thermoforming of single and multilayer laminates, in: Plastic Films Technologies, Testing, And Applications, Vol 7, Elsevier, 2019, pp. 147–192, https://doi.org/10.1016/B978-0-12-814523-4.00004-6.
[33] X. Liang, J. Gao, W. Xu, et al., Structural mechanics of 3D-printed poly(lactic acid) scaffolds with tetragonal, hexagonal and wheel-like designs, Biofabrication 11 (3) (2019), 035009, https://doi.org/10.1088/1758-5090/ab0f59.

[34] S.D. McCullen, H. Autefage, A. Callanan, E. Gentleman, M.M. Stevens, Anisotropic fibrous scaffolds for articular cartilage regeneration, Tissue Eng. A 18 (19–20) (2012) 2073–2083, https://doi.org/10.1089/ten.tea.2011.0606.
[35] J.A.M. Steele, S.D. McCullen, A. Callanan, et al., Combinatorial scaffold morphologies for zonal articular cartilage engineering, Acta Biomater. 10 (5) (2014) 2065–2075, https://doi.org/10.1016/j.actbio.2013.12.030.
[36] J. Feng, T. Hu, W. Liu, et al., The biomechanical, morphologic, and histochemical properties of the costal cartilages in children with pectus excavatum, J. Pediatr. Surg. 36 (12) (2001) 1770–1776, https://doi.org/10.1053/jpsu.2001.28820.
[37] S. Provot, E. Schipani, Molecular mechanisms of endochondral bone development, Biochem. Biophys. Res. Commun. 328 (3) (2005) 658–665, https://doi.org/10.1016/j.bbrc.2004.11.068.
[38] A.J. Engler, S. Sen, H.L. Sweeney, D.E. Discher, Matrix elasticity directs stem cell lineage specification, Cell 126 (4) (2006) 677–689, https://doi.org/10.1016/j.cell.2006.06.044.
[39] A. Lau, M.L. Oyen, R.W. Kent, D. Murakami, T. Torigaki, Indentation stiffness of aging human costal cartilage, Acta Biomater. 4 (1) (2008) 97–103, https://doi.org/10.1016/j.actbio.2007.06.008.
[40] D.D. Deligianni, A. Maris, Y.F. Missirlis, Stress relaxation behaviour of trabecular bone specimens, J. Biomech. 27 (12) (1994) 1469–1476, https://doi.org/10.1016/0021-9290(94)90196-1.
[41] S.H. Park, E.S. Gil, B.B. Mandal, et al., Annulus fibrosus tissue engineering using lamellar silk scaffolds, J.Tissue Eng.Regen.Med. (2012), https://doi.org/10.1002/term.541.
[42] J.C. Moses, S.K. Nandi, B.B. Mandal, Multifunctional cell instructive silk-bioactive glass composite reinforced scaffolds toward osteoinductive, proangiogenic, and resorbable bone grafts, Adv.Healthc.Mater. (2018), https://doi.org/10.1002/adhm.201701418.
[43] C.M. Murphy, F.J. O'Brien, Understanding the effect of mean pore size on cell activity in collagen-glycosaminoglycan scaffolds, Cell Adhes.Migr. 4 (3) (2010) 377–381, https://doi.org/10.4161/cam.4.3.11747.
[44] K. Zhang, Y. Fan, N. Dunne, X. Li, Effect of microporosity on scaffolds for bone tissue engineering, Regen.Biomater. 5 (2) (2018) 115–124, https://doi.org/10.1093/rb/rby001.
[45] J. Rosser, L. Bonewald, Bone research protocols: studying osteocyte function using the cell lines MLO-Y4 and MLO-A5 Vol 816, 2012.
[46] D. Gothard, K. Cheung, J.M. Kanczler, D.I. Wilson, R.O.C. Oreffo, Regionally-derived cell populations and skeletal stem cells from human foetal femora exhibit specific osteochondral and multi-lineage differentiation capacity in vitro and ex vivo, Stem Cell Res.Ther. 6 (1) (2015) 1–17, https://doi.org/10.1186/s13287-015-0247-2.
[47] P. Nowak-Sliwinska, T. Segura, M.L. Iruela-Arispe, The chicken chorioallantoic membrane model in biology, medicine and bioengineering, Angiogenesis 17 (4) (2014) 779–804, https://doi.org/10.1007/s10456-014-9440-7.
[48] P. Nowak-Sliwinska, K. Alitalo, E. Allen, et al., Consensus Guidelines for the Use And Interpretation of Angiogenesis Assays Vol 21, Springer, Netherlands, 2018, https://doi.org/10.1007/s10456-018-9613-x.
[49] D.D. Bikle, Vitamin D metabolism, mechanism of action, and clinical applications, Chem. Biol. 21 (3) (2014) 319–329, https://doi.org/10.1016/j.chembiol.2013.12.016.
[50] C. Wang, H. Meng, X. Wang, C. Zhao, J. Peng, Y. Wang, Differentiation of bone marrow mesenchymal stem cells in osteoblasts and adipocytes and its role in treatment of osteoporosis, Med. Sci. Monit. 22 (2016) 226–233, https://doi.org/10.12659/MSM.897044.
[51] W. Huang, B. Carlsen, G. Rudkin, et al., Osteopontin is a negative regulator of proliferation and differentiation in MC3T3-E1 pre-osteoblastic cells, Bone 34 (5) (2004) 799–808, https://doi.org/10.1016/j.bone.2003.11.027.
[52] J.A. McGovern, M. Griffin, D.W. Hutmacher, Animal models for bone tissue engineering and modelling disease, Dis. Model. Mech. 11 (4) (2018), dmm033084, https://doi.org/10.1242/dmm.033084.
[53] S. Ghanaati, R.E. Unger, M.J. Webber, et al., Scaffold vascularization in vivo driven by primary human osteoblasts in concert with host inflammatory cells, Biomaterials 32 (32) (2011) 8150–8160, https://doi.org/10.1016/j.biomaterials.2011.07.041.
[54] M. Pereira, E. Petretto, S. Gordon, J.H.D. Bassett, G.R. Williams, J. Behmoaras, Common signalling pathways in macrophage and osteoclast multinucleation, J. Cell Sci. 131 (11) (2018), jcs216267, https://doi.org/10.1242/jcs.216267.
[55] E. Jabbarzadeh, T. Starnes, Y.M. Khan, et al., Induction of angiogenesis in tissue-engineered scaffolds designed for bone repair: a combined gene therapy-cell transplantation approach, Proc. Natl. Acad. Sci. U. S. A. 105 (32) (2008) 11099–11104, https://doi.org/10.1073/pnas.0810217105.
[56] Z. Shirbaghaee, M. Hassani, S. Heidari Keshel, M. Soleimani, Emerging roles of mesenchymal stem cell therapy in patients with critical limb ischemia, Stem Cell Res. Ther. 13 (1) (2022) 462, https://doi.org/10.1186/s13287-022-03148-9.
[57] D. Tang, R.S. Tare, L.Y. Yang, D.F. Williams, K.L. Ou, R.O.C. Oreffo, Biofabrication of bone tissue: approaches, challenges and translation for bone regeneration, Biomaterials 83 (2016) 363–382, https://doi.org/10.1016/j.biomaterials.2016.01.024.
[58] R.A.D. Carano, E.H. Filvaroff, Angiogenesis and bone repair, Drug Discov. Today 8 (21) (2003) 980–989, https://doi.org/10.1016/S1359-6446(03)02866-6.
[59] B. Clarke, Normal bone anatomy and physiology, Clin.J.Am.Soc.Nephrol. 3 (Suppl 3) (2008) 131–139, https://doi.org/10.2215/CJN.04151206.
[60] R. Marsell, T.A. Einhorn, The biology of fracture healing, Injury 42 (6) (2011) 551–555, https://doi.org/10.1016/j.injury.2011.03.031.
[61] J.P. Vacanti, R. Langer, Tissue engineering: the design and fabrication of living replacement devices for surgical reconstruction and transplantation, Lancet 354 (1999) 32–34, https://doi.org/10.1016/s0140-6736(99)90247-7.
[62] B. Dhandayuthapani, Y. Yoshida, T. Maekawa, D.S. Kumar, Polymeric scaffolds in tissue engineering application: a review, Int.J.Polym.Sci. (2011), https://doi.org/10.1155/2011/290602.
[63] N.A. Nawawi, A.S.F. Alqap, I. Sopyan, Recent progress on hydroxyapatite-based dense biomaterials for load bearing bone substitutes, Recent Pat Mater. Sci. 4 (1) (2011) 63–80, https://doi.org/10.2174/1874465611104010063.
[64] C.B. Khatiwala, S.R. Peyton, M. Metzke, A.J. Putnam, The regulation of osteogenesis by ECM rigidity in MC3T3-E1 cells requires MAPK activation, J. Cell. Physiol. 211 (2007) 661–672, https://doi.org/10.1002/jcp.20974.
[65] R.O. Navarrete, E.M. Lee, K. Smith, et al., Substrate stiffness controls osteoblastic and chondrocytic differentiation of mesenchymal stem cells without exogenous stimuli, PLoS ONE 12 (1) (2017) 1–18, https://doi.org/10.1371/journal.pone.0170312.
[66] H. Gerardo, A. Lima, J. Carvalho, et al., Soft culture substrates favor stem-like cellular phenotype and facilitate reprogramming of human mesenchymal stem/stromal cells (hMSCs) through mechanotransduction, Sci. Rep. 9 (1) (2019) 1–18, https://doi.org/10.1038/s41598-019-45352-3.
[67] F. Rossi, M. Santoro, G. Perale, Polymeric scaffolds as stem cell carriers in bone repair, J. Tissue Eng. Regen. Med. 9 (10) (2015) 1093–1119, https://doi.org/10.1002/term.1827.
[68] V. Moulisová, C. Gonzalez-García, M. Cantini, et al., Engineered microenvironments for synergistic VEGF – integrin signalling during vascularization, Biomaterials 126 (2017) 61–74, https://doi.org/10.1016/j.biomaterials.2017.02.024.
[69] A. Ambesi, P.J. McKeown-Longo, Conformational remodeling of the fibronectin matrix selectively regulates VEGF signaling, J. Cell Sci. 127 (17) (2014) 3805–3816, https://doi.org/10.1242/jcs.150458.
[70] F. Villars, L. Bordenave, R. Bareille, J. Amde, Effect of human endothelial cells on human bone marrow stromal cell phenotype: role of VEGF? J. Cell. Biochem. 79 (4) (2000) 672–685, https://doi.org/10.1002/1097-4644(20001215)79:4<672::AID-JCB150>3.0.CO;2-2.
[71] A. Cardus, S. Panizo, M. Encinas, et al., 1,25-Dihydroxyvitamin D3 regulates VEGF production through a vitamin D response element in the VEGF promoter, Atherosclerosis 204 (1) (2009) 85–89, https://doi.org/10.1016/j.atherosclerosis.2008.08.020.
[72] S.P. Timoshenko, J.N. Goodier, Theory of elasticity. Chapter 1, in: McGraw-Hill (Ed.), Theory of Elasticity, 3rd ed., 1951, pp. 1–14.
[73] M. van Driel, J.P.T.M. van Leeuwen, Vitamin D endocrine system and osteoblasts, BoneKEy Rep. 3 (February) (2014) 1–8, https://doi.org/10.1038/bonekey.2013.227.
[74] F. Langenbach, J. Handschel, Effects of dexamethasone, ascorbic acid and β-glycerophosphate on the osteogenic differentiation of stem cells in vitro, Stem Cell Res. Ther. 4 (5) (2013) 117–430, https://doi.org/10.1089/ten.teb.2011.0199.
[75] C. Fu, D. Luo, M. Yu, et al., Embryonic-like mineralized extracellular matrix/stem cell microspheroids as a bone graft substitute, Adv. Healthc. Mater. 1800705 (2018), 1800705, https://doi.org/10.1002/adhm.201800705.
[76] S. Inglis, K.H. Schneider, J.M. Kanczler, H. Redl, R.O.C. Oreffo, Harnessing human decellularized blood vessel matrices and cellular construct implants to promote bone healing in an ex vivo organotypic bone defect model, Adv.Healthc.Mater. 1800088 (2018) 1–12, https://doi.org/10.1002/adhm.201800088.